Supplement of Hydrol. Earth Syst. Sci., 30, 5195–5214, 2026
https://doi.org/10.5194/hess-30-5195-2026-supplement

Hydrology and Earth System Sciences
Open Access

Supplement of

Hydrologic model parameter estimation in snow-dominated headwater catchments using multiple observation datasets

Lauren H. North et al.

Correspondence to: Lauren H. North (north@mines.edu)

Contents of this file

Text S1 to S3
Figures S1 to S16
Tables S1 to S4

Introduction

This document provides supplementary information on data processing, model details, study catchment details, and the results of the Morris sensitivity analysis and LHS Monte Carlo filtering. The MODIS snow-covered area observations (Text S1) and soil moisture observations (Text S2) required transformations and quality checks before use in model comparison. The definitions of Morris sensitivity indices, as well as the bootstrapping procedure is described in detail (Text S3). Model parameter definitions and the study catchments are described in table S1 and S2, respectively. The number of sensitive parameters identified via the Morris methods described comprehensively in table S3. The results from baseline NHM parameters sets are shown in table S4. Figures S2 - S10, in addition to S16 pertain to the Morris sensitivity analysis. Figures 11-15 are pertain to the LHS Monte Carlo filtering for evaluation of model performance and parameter estimation.

S1

The following text describes the data transformations performed on the MODIS snow covered area product used in this study (MOD10A1.061). The model output *snowcov_area* returns a value ranging from 0 to 1, representing the fractional snow-covered area (fSCA) in each HRU. The raw data from the MOD10A1 product is normalized difference snow index (NDSI) ranging from 0 to 100, which was first changed from a percentage to a 0 to 1 ratio. Then, it was converted to fSCA using the recommended universal transformation (equation 1) from (Salomonson & Appel, 2004). The 500-meter resolution data is then aggregated by HRU.

$$fSCA = 0.06 + (1.21 * NDSI) \tag{S1}$$

While the method above was created for the deprecated MODIS collection 5 products, it remains appropriate for collection 6 products (Hall et al., 2019; Stillinger et al., 2023). Any fSCA values returned from equation 1 that are greater than 1.0 were set to 1.0. Additionally, values less than or equal to 0.1 were not included in the model evaluation due to the associated uncertainty of the transformation, and to not credit the model performance for predicting zeros (i.e. in the summer). Previous PRMS analyses filter the MODIS data using confidence intervals published with the dataset (Hay et al., 2023); however, that was not provided in the MOD10A1.061 product available on Google Earth Engine, which we use preferentially here to facilitate reproducibility.

S2

The following text describes the *in situ* soil moisture observations and pre-screening done in this study. The soil moisture sensors at NRCS SNOTEL stations are at 2 cm, 8 cm, and 20 cm depths, abbreviated as SMS2, SMS8, and SMS20. The raw data contains values largely ranging from 0 to 0.5, with a few error values removed. Soil moisture (volumetric water content, q) ranges from 0 to φ , where φ represents porosity and ranges from 0.3 to 0.55 for most soils (Dingman, 2015). Therefore, the volumetric water content observed by the *in situ* SNOTEL sensors can be converted to saturation (wetness) Q, by dividing by the maximum observed q in a timeseries of *t* timesteps (equation S1):

$$\Theta_t = \frac{\theta_t}{\mathrm{f}} \cong \frac{\theta_t}{\max(\theta_t)} \tag{S2}$$

S3

The following text describes the Morris method and bootstrapping in detail. The modeler must make two decisions in the design of the Morris experiment, p levels and r trajectories. The levels determine the step size of the parameter values, discretizing the *k*-dimensional parameter space by setting them to intervals of $1/(p-1)$. The trajectories represent the number of times in which the Elementary Effects are calculated, where each trajectory (j) starts at a random point in the *p* gridded parameter space. Let x_i be an individual parameter in a vector of parameters, $\boldsymbol{X}$, that contains a total of k parameters ($i = 1,2, \ldots, k$). The elementary effect for each parameter, EE_i, is calculated by assessing the difference in the output function f due to the perturbation Δ to parameter x_i, relative to the output where x_i is fixed (noted by $f(\boldsymbol{X}|_{x_i}^{j})$ in equation S3). The perturbation Δ is a fraction of the parameters range determined by $p/(2(p-1))$. The recommended value of *p* is at least 8, which is used in this study (Gan et al., 2014). The output function in our study is NRMSE as described in section 2.4.

$$EE_i^j = \frac{f\left(x_1^j, \ldots, x_i^j + \Delta, \ldots, x_k^j\right) - f(\boldsymbol{X}|_{x_i}^{j})}{\Delta} \tag{S3}$$

Two measures of sensitivity are proposed by (Morris, 1991): these are, μ_i, which represents the overall influence of the input factor, and σ_i, which represents the factor's higher-order effects (non-linearity or interactions with other factors). These two measures are the mean and standard deviation of the elementary effects over *r* total trajectories. In each *j* trajectory, each parameter is perturbed once. The measure μ_i may be positive or negative depending on the model's response. By taking the absolute value (denoted as μ^* in equation S4) the metric is better suited for ranking and screening procedures (Campolongo et al., 2007).

$$\mu_i^* = \frac{1}{r} \sum_{j=1}^{r} |EE_i^j| \tag{S4}$$

The typical number of trajectories (*r*) is 10; however, some have noted the inherent reliability issues associated with deriving a mean sensitivity measure from a sample of 10 (Gan et al., 2014). Cuntz et al. (2015) recommends the number of trajectories be at least the number of parameters to achieve stable sensitivity measures. Given the 51 parameters used in this study (*k*), we follow this recommendation and use *r* equal to 51 trajectories. The number of model evaluations (N) is a function of k and r (equation S5), resulting in 2652 model runs for each catchment.

$$N = r * (k+1) \tag{S5}$$

Even with a sufficient number of trajectories, uncertainty remains associated with the sensitivity measure μ^*. For that reason, we bootstrap the sensitivity measures – which involves replacement resampling of the elementary effects, a vector of length of *r* for each parameter (i) (Campolongo & Saltelli, 1997). The sensitivity measure is calculated for each *b* bootstrap sample μ_i^{*b}, then averaged over a total of *B* samples to yield the bootstrap mean, $\overline{\mu_i^{*b}}$ (equation S6). In this study, we use *B = 1000* bootstrap replicates.

$$\overline{u_i^{*b}} = \frac{1}{B} \sum_{b=1}^{B} u_i^{*b} \tag{S6}$$

Since the results of the bootstrap are normally distributed, the uncertainty can be determined by calculating the standard deviation of the bootstrap ($SD(\mu_i^*)$ in equation S7) and placing that as a bound on the bootstrap mean (±1.0*SD for 66%, ±1.95*SD for 95%).

$$SD(\mu_i^*) = \sqrt{\frac{1}{B-1} \sum_{b=1}^{B} (u_i^{*b} - \overline{u_i^{*b}})^2} \tag{S7}$$

To facilitate the screening of informative parameters, a normalized measure ranging from 0 to 1 called η^* is found by dividing the elementary effect of each parameter (μ_i^*) by the maximum elementary effect of the set of parameters (μ_{max}^*), shown in equation S8.

$$\eta_i^* = \frac{\overline{u_i^{*b}}}{\max(\overline{u_i^{*b}})} \tag{S8}$$

To determine which parameters are non-informative versus informative, a threshold value for η^* is established (η_{thresh}^*). We use the sigmoidal logistic function defined in (Cuntz et al., 2015) to determine η_{thresh}^*. If the calculated η_{thresh}^* is greater than 0.2, it is set to 0.2. When a parameter is denoted informative, it is carried forward into the Monte Carlo filtering framework. For parameters denoted as non-informative, their NHM default values are fixed and excluded from further analysis. Some η_i^* values are near the threshold values, and the results of the bootstrapping allow for the identification of type I and type II statistical errors. We use a confidence bound of $\overline{\mu_i^{*b}} \pm 1.0 * SD(\mu_i^*)$ in the numerator of equation 2.9 to derive error bounds for the η_i^* metric. A type I error occurs when η_i^* is above the threshold, but the lower bound is below it (false positive). A type II errors occurs when η_i^* is below the threshold, but the upper uncertainty bound is above it (false negative). Generally, screening methods ought to be robust to type II errors, but these may occur when a model response is non monotonic resulting in a low μ^* but with high variability (Saltelli et al., 2007). When type II errors occur, the parameter is treated as informative and included in the LHS analysis.

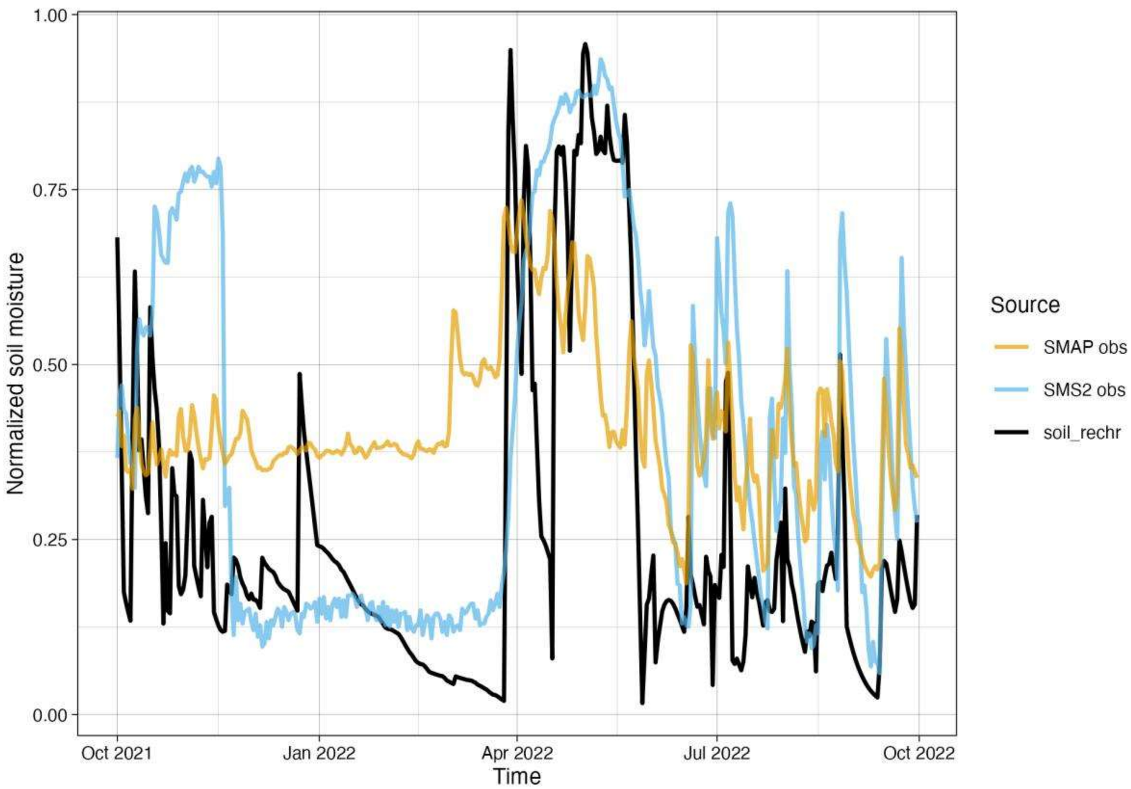

Figure S1. An example timeseries of normalized soil moisture from remotely sensed SMAP, an *in-situ* sensor at 2 cm depth (SMS2), and the simulated output (*soil_rechr*) using the NHM parameter set. The simulated output and SMAP are areal averages pertaining to the same hydrologic response unit where the *in situ* sensor is located (station 380 in the East River).

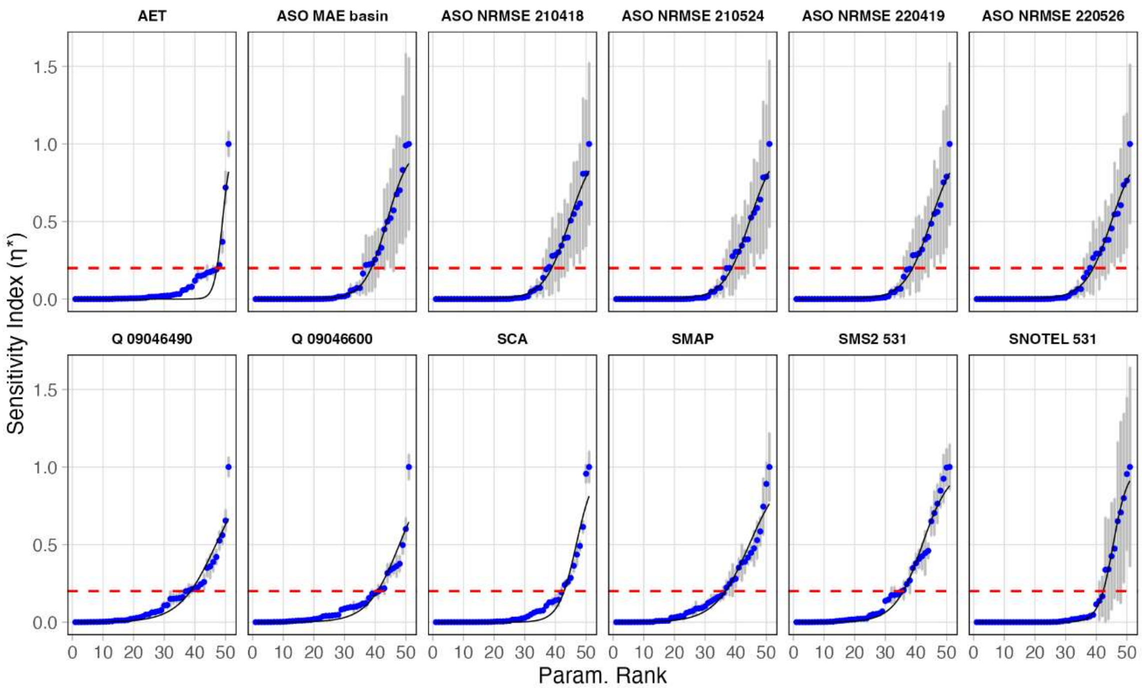

Figure S2. Fitted logistic function to the bootstrapped normalized sensitivity metric η_i^* for each *in situ* and remotely sensed data sets in the *Blue River*. Error bounds shown in gray are estimated from the bootstrap variability, $\pm 1.0 * SD(\mu_i^*)$.

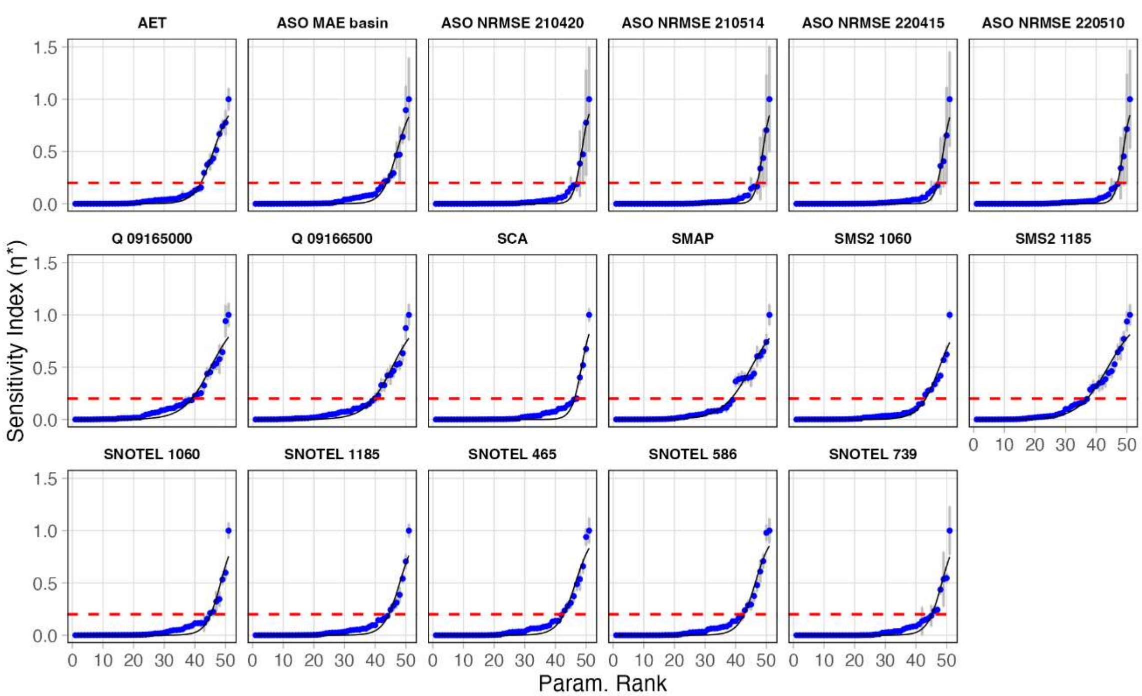

Figure S3. Fitted logistic function to the bootstrapped normalized sensitivity metric η_i^* for each *in situ* and remotely sensed data sets in the *Dolores River*. Error bounds shown in gray are estimated from the bootstrap variability, $\pm 1.0 * SD(\mu_i^*)$.

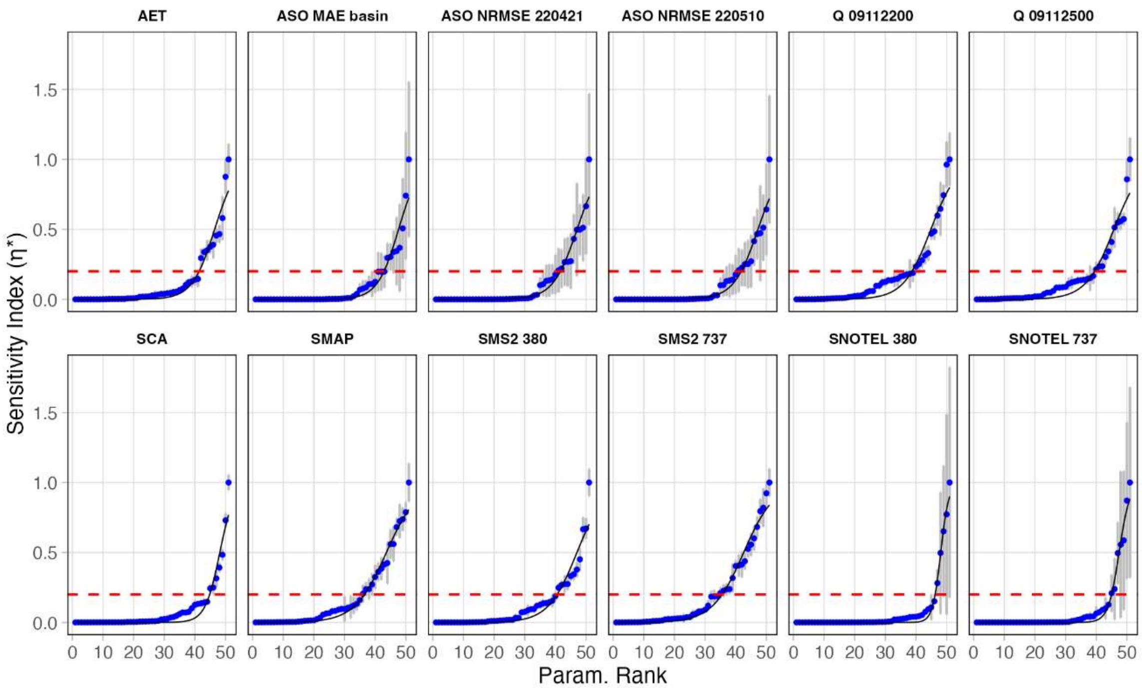

Figure S4. Fitted logistic function to the bootstrapped normalized sensitivity metric η_i^* for each *in situ* and remotely sensed data sets in the *East River*. Error bounds shown in gray are estimated from the bootstrap variability, $\pm 1.0 * SD(\mu_i^*)$.

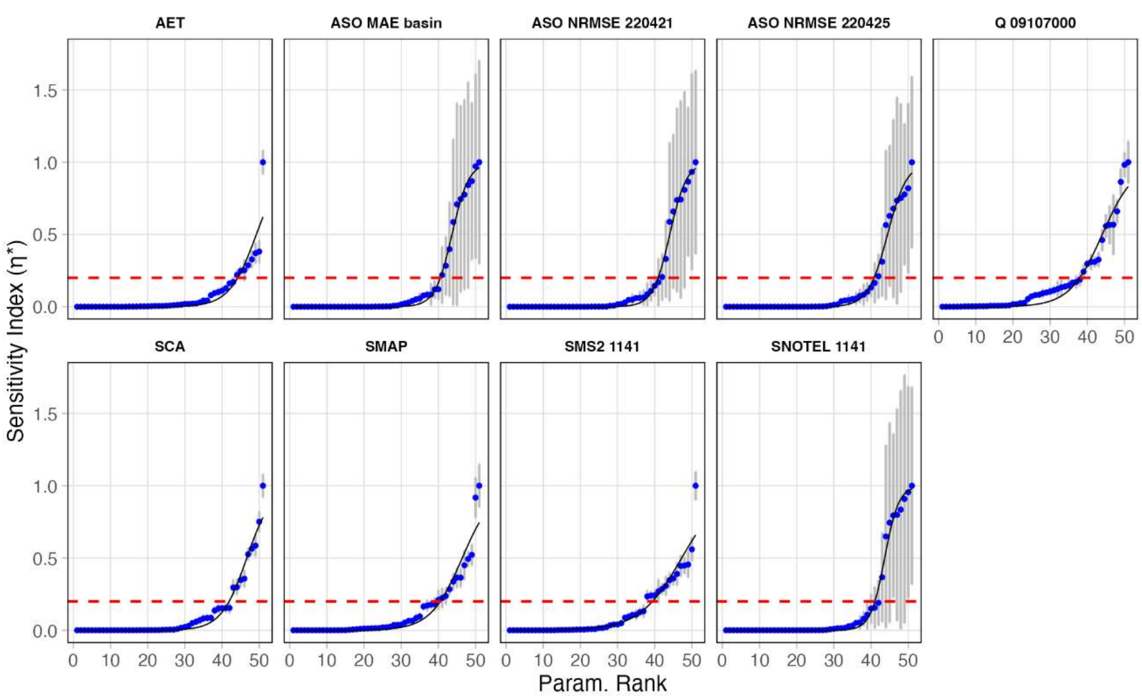

Figure S5. Fitted logistic function to the bootstrapped normalized sensitivity metric η_i^* for each *in situ* and remotely sensed data sets in the *Taylor River*. Error bounds shown in gray are estimated from the bootstrap variability, $\pm 1.0 * SD(\mu_i^*)$.

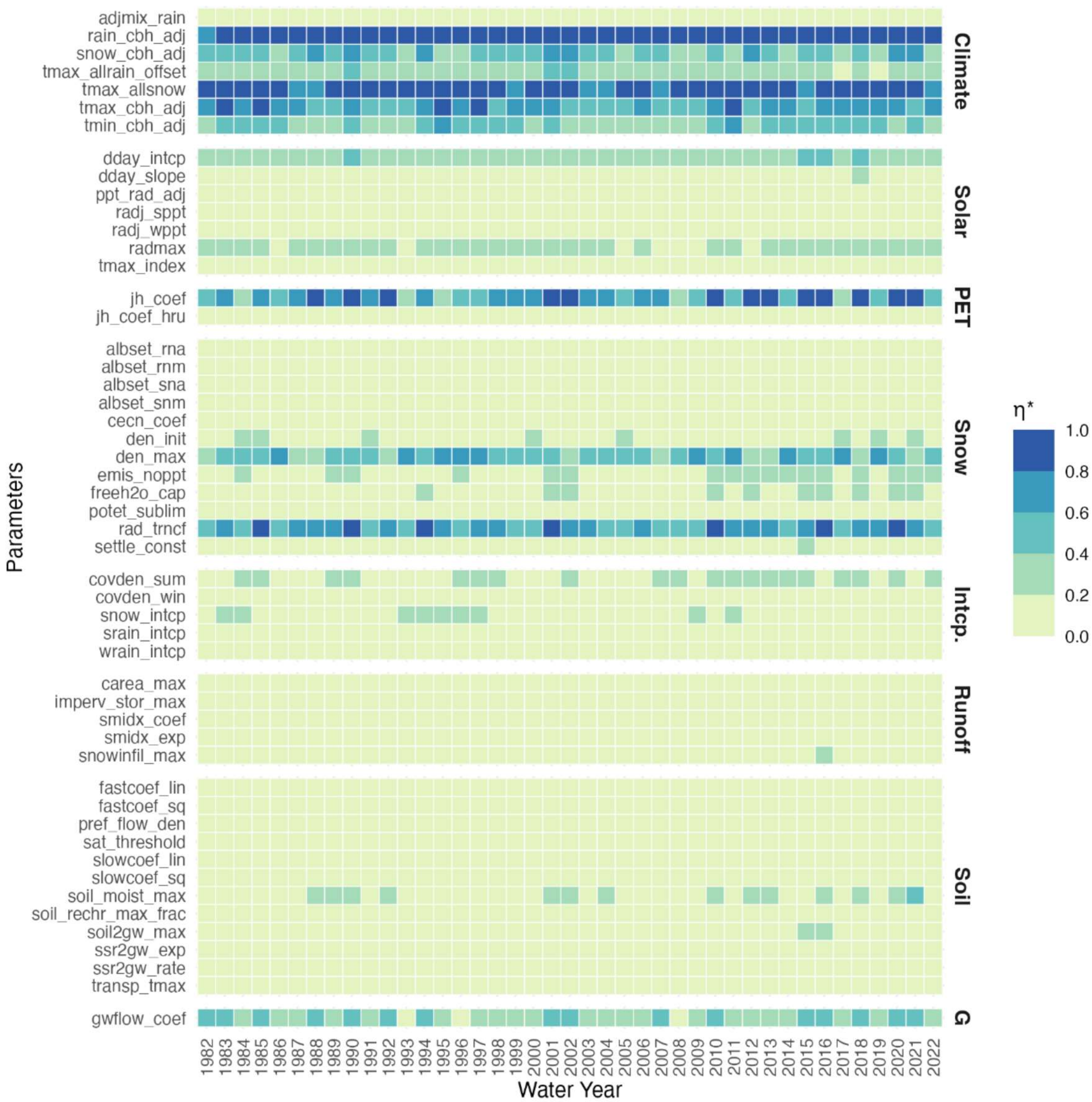

Figure S6. A heatmap showing $\boldsymbol{\eta}^*$ for annual moving windows based on NRMSE of Q at USGS 09112500 in the East River Basin.

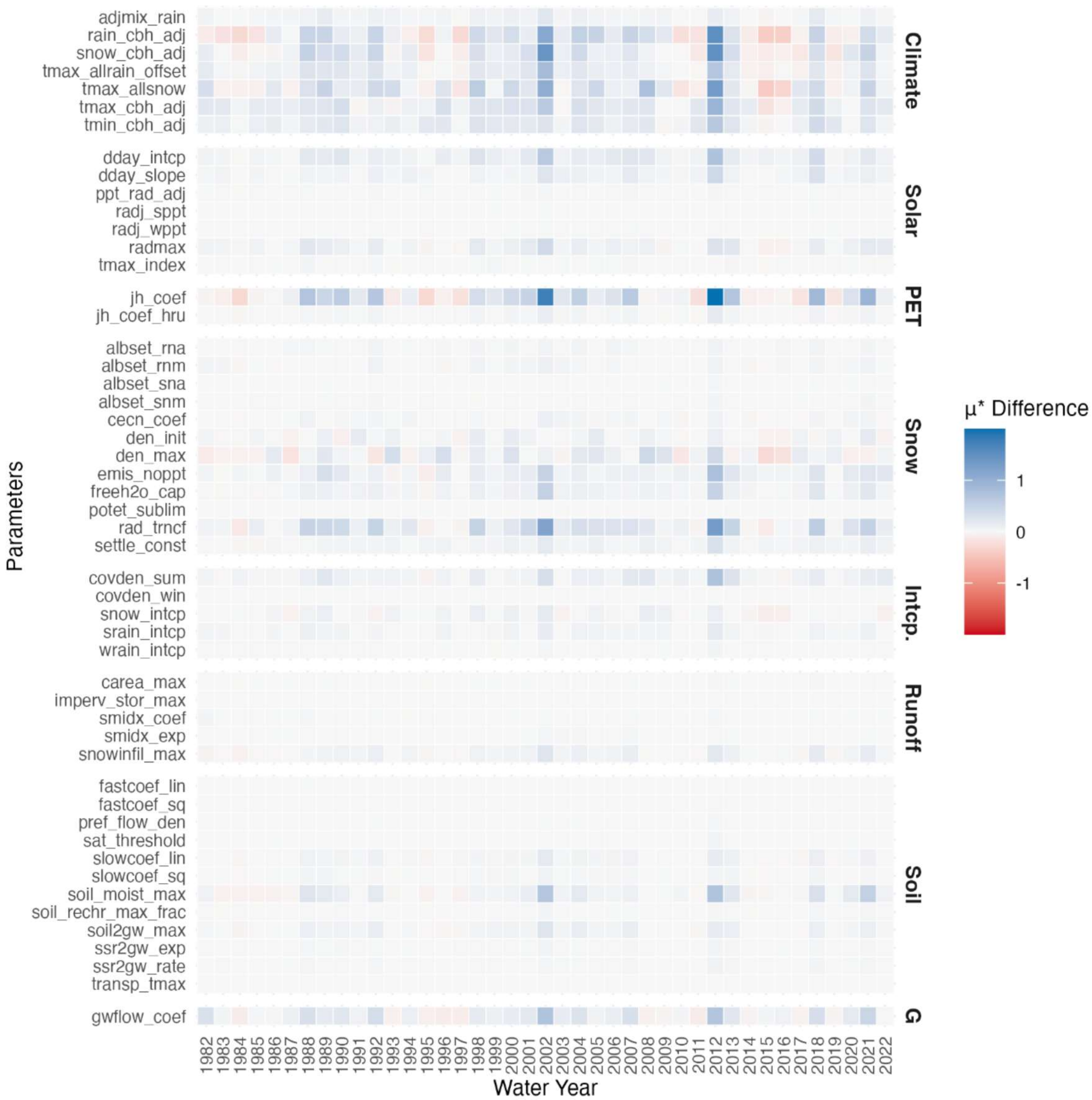

Figure S7. A heatmap showing the *difference* in $\boldsymbol{\mu}^*$ between annual moving windows and the full period (1982-2022). The sensitivity metric $\boldsymbol{\mu}^*$ is calculated based on NRMSE of Q at USGS 09112500 in the East River Basin.

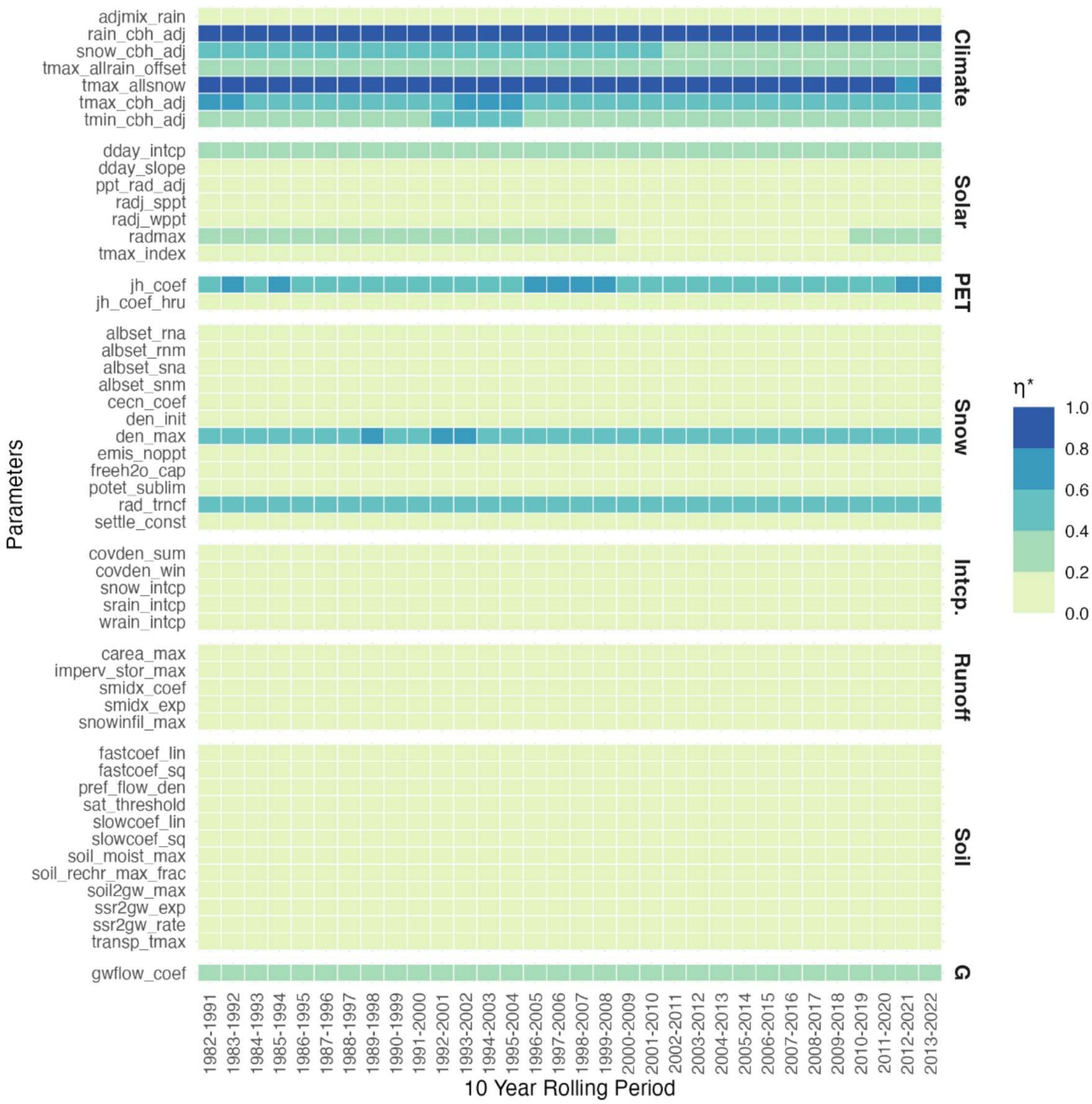

Figure S8. A heatmap showing $\boldsymbol{\eta}^{*}$ for 10-year moving windows based on NRMSE of Q at USGS 09112500 in the East River Basin.

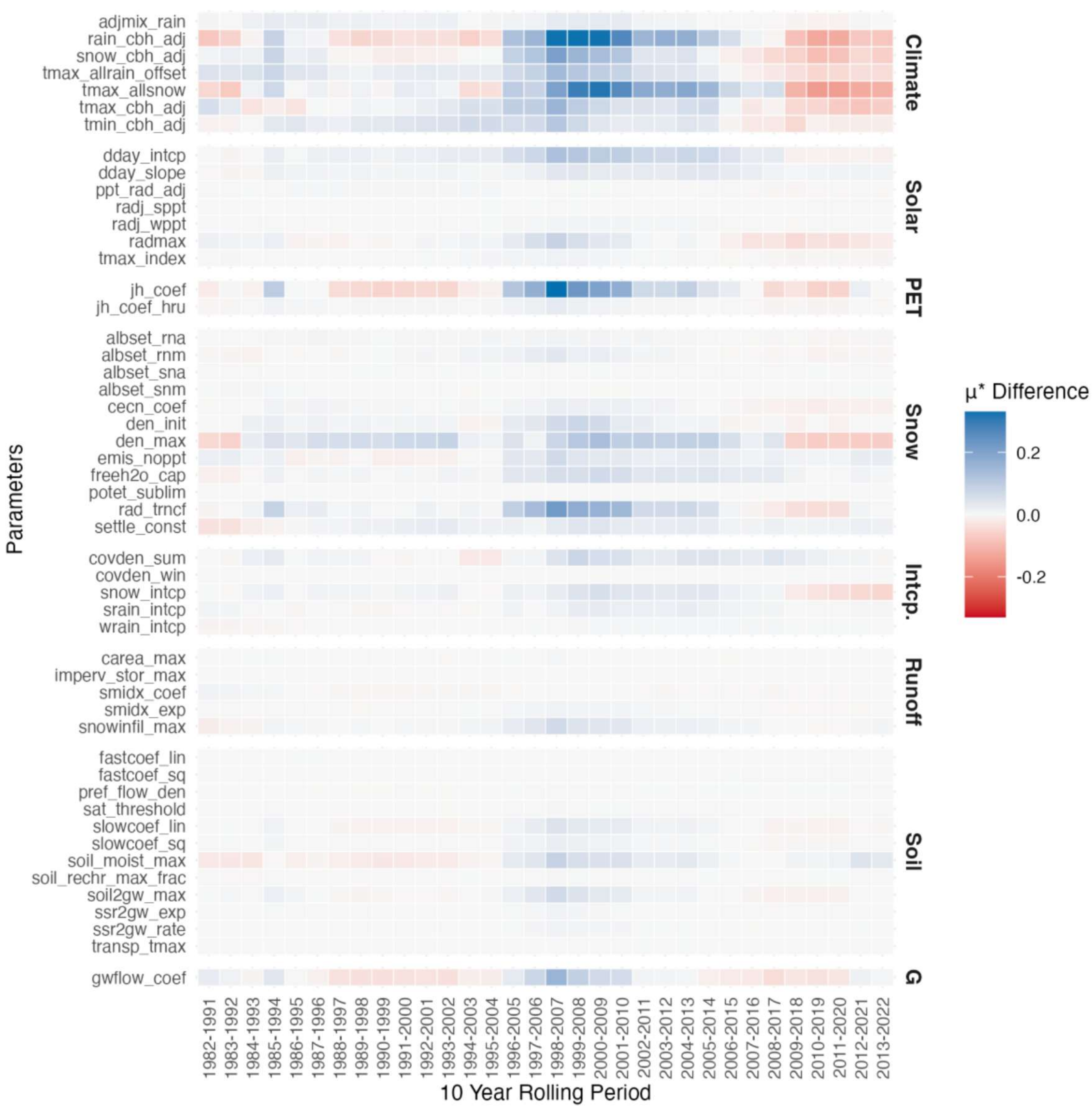

Figure S9. A heatmap showing the *difference* in $\boldsymbol{\mu}^*$ between 10-year moving windows and the full period (1982-2022). The sensitivity metric $\boldsymbol{\mu}^*$ is calculated based on NRMSE of Q at USGS 09112500 in the East River Basin.

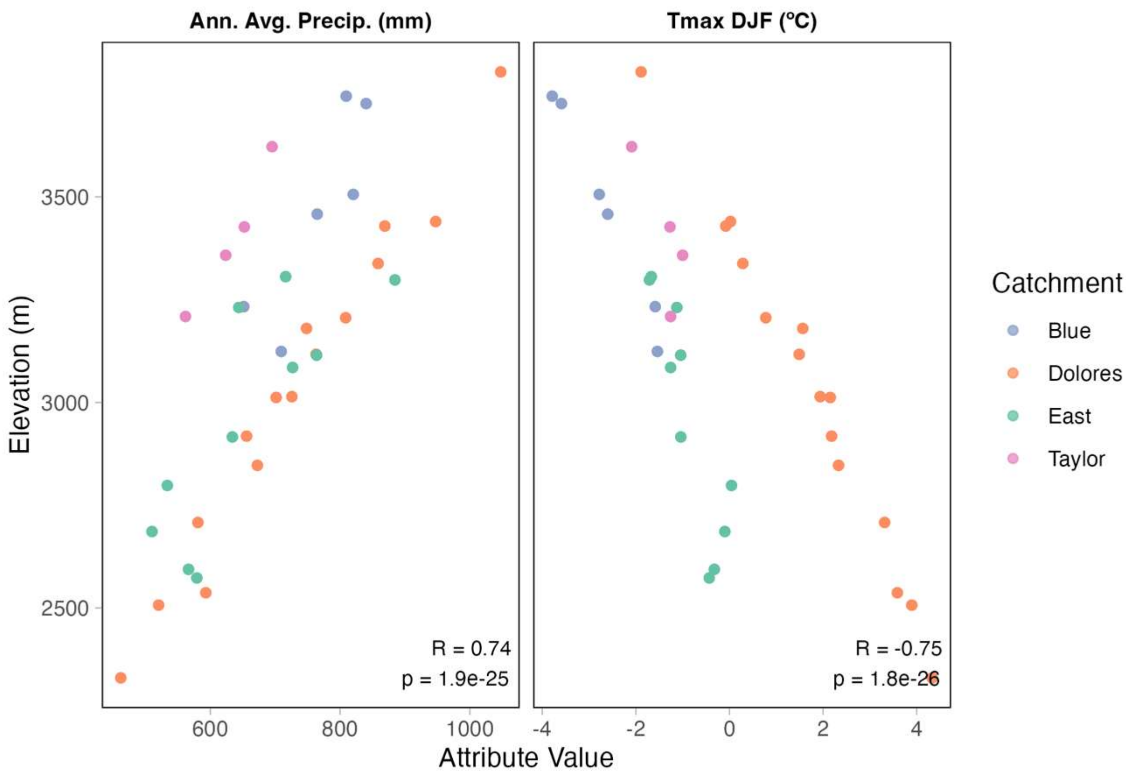

Figure S10. The relationship between HRU elevation and average forcing inputs over water years 1982-2022.

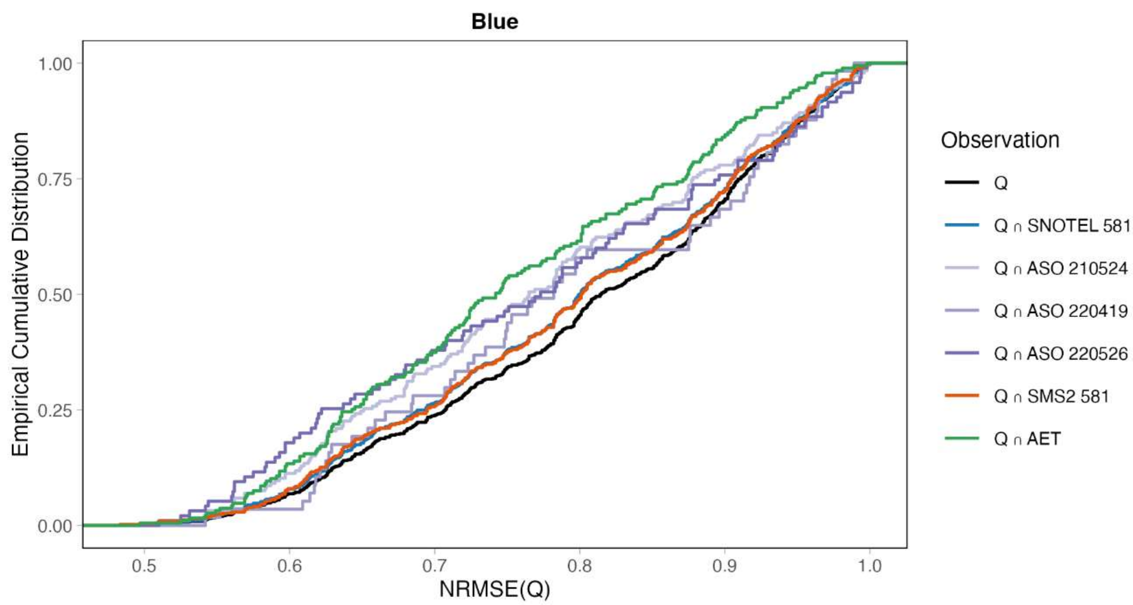

Figure S11. Empirical cumulative distribution function of NRMSE of discharge for all data locations and types in the Blue River. All intersections with n > 30 are shown.

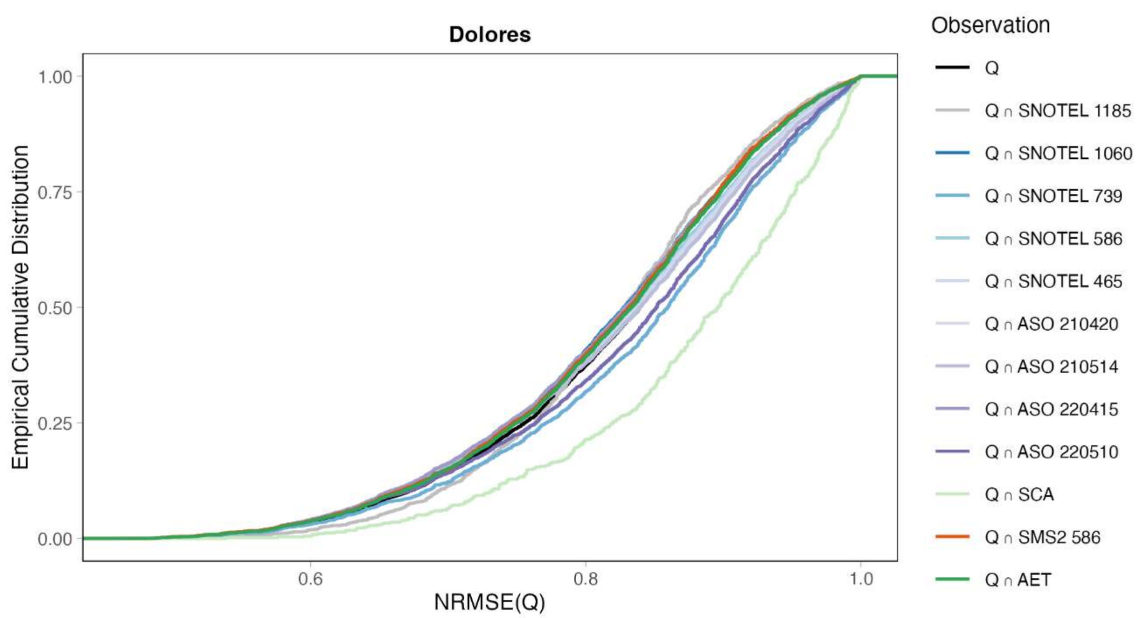

Figure S12. Empirical cumulative distribution function of NRMSE of discharge for all data locations and types in the Dolores River. All intersections with n > 30 are shown.

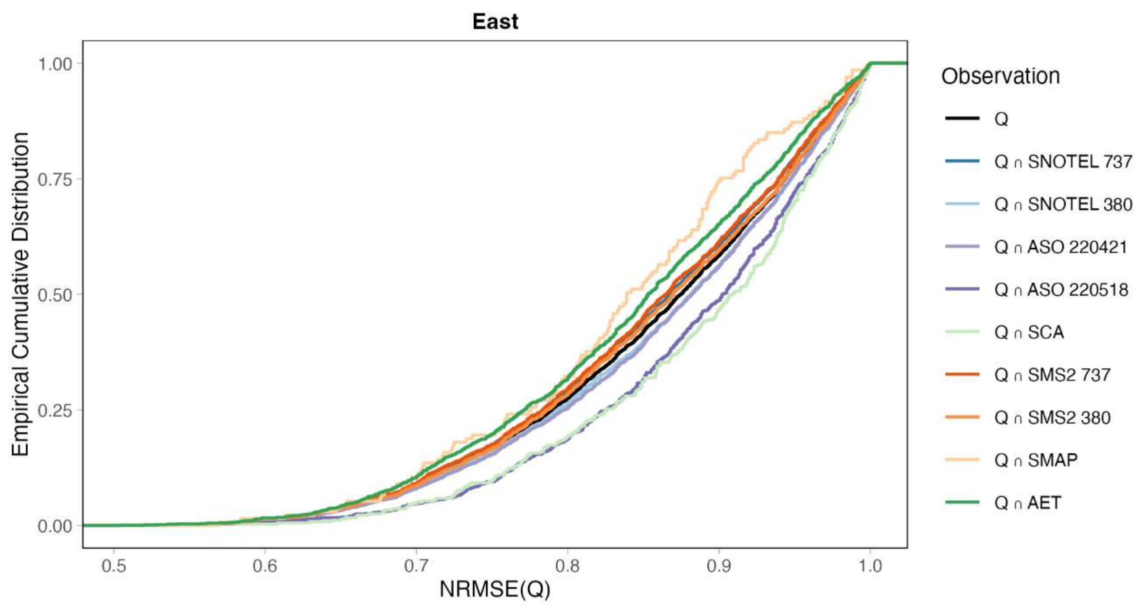

Figure S13. Empirical cumulative distribution function of NRMSE of discharge for all data locations and types in the East River. All intersections with n > 30 are shown.

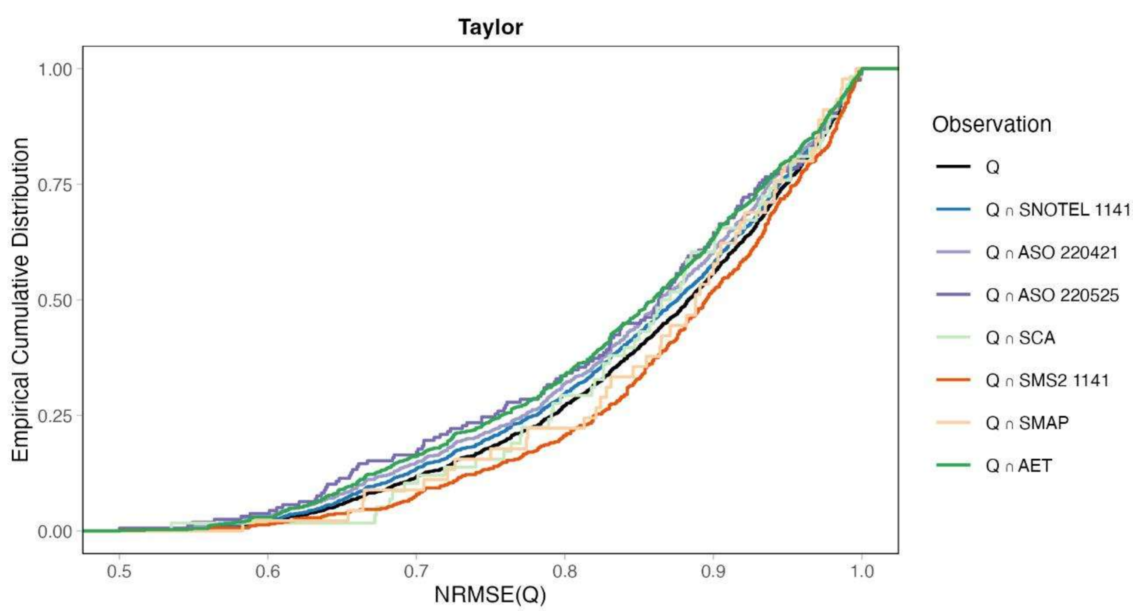

Figure S14. Empirical cumulative distribution function of NRMSE of discharge for all data locations and types in the Taylor River. All intersections with n > 30 are shown.

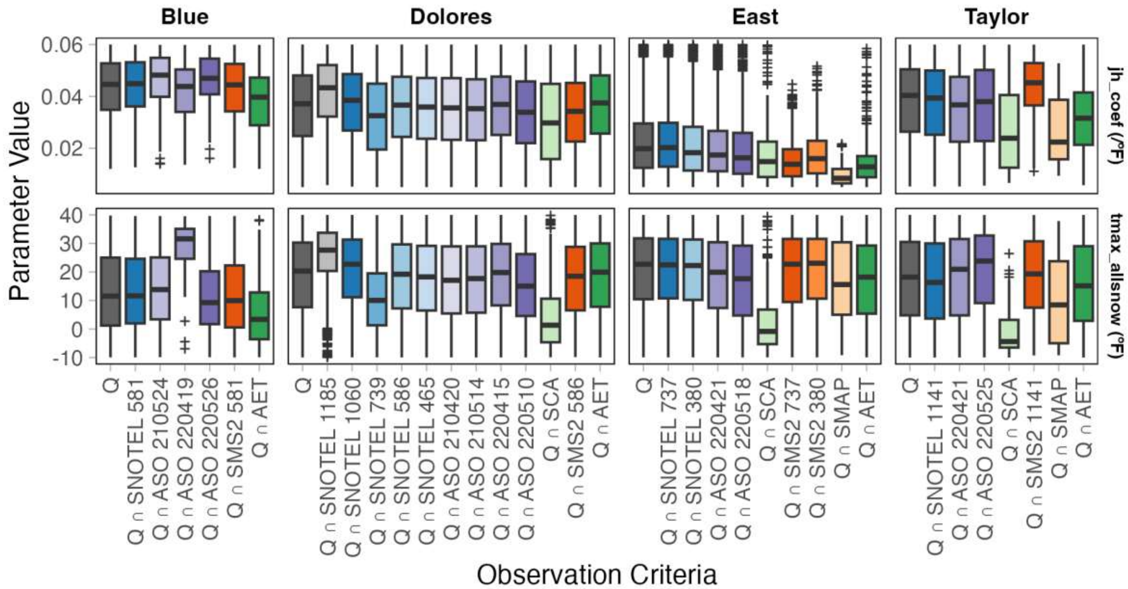

Figure S15. The inter-quartile ranges of behavioral parameter values fluctuate across observation data criteria. For catchments that have more than one stream gauge, the behavioral intersection of both was taken. All intersections with n > 30 are shown.

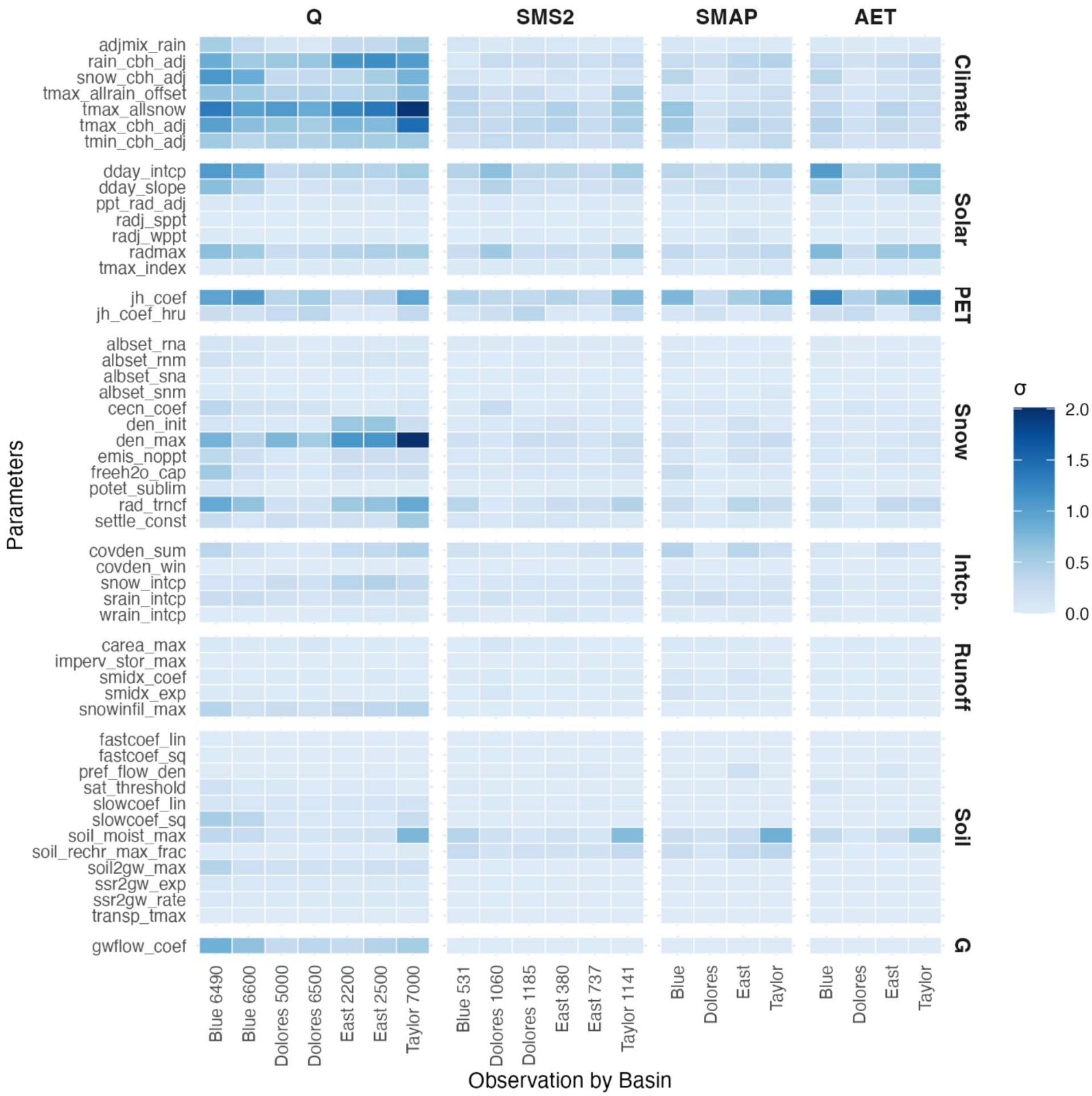

Figure S16. A heatmap showing the Morris parameter interaction and nonlinearity term $\boldsymbol{\sigma}$ for relevant observations available from WY 1982 through 2022. The snow datasets are excluded due to high values that skew the data interpretation.

Table S1. Description of PRMS/pywatershed parameters selected for sensitivity analysis and calibration. The selection was based on prior literature where source 1 = Markstrom et al., 2016; 2 = Hay et al., 2023; 3 = Mei et al., 2023; 4 = Douglas-Mankin & Moser, 2019; and 5 = this manuscript.

Parameter Name	Description	PRMS Module	Units	Range	Source
adjmix_rain	Monthly factor to adjust rain proportion in a mixed rain/snow event	Climate	decimal fraction	0.6 to 1.4	1, 2, 3
rain_cbh_adj	Monthly adjustment factor to measured precipitation on each HRU	Climate	decimal fraction	0.5 to 2.0	2
snow_cbh_adj	Monthly adjustment factor to measured precipitation on each HRU	Climate	decimal fraction	0.5 to 2.0	2, 3
tmax_allrain_offset	Monthly maximum air temperature when precipitation is assumed to be rain	Climate	˚F	-8 to 60	2
tmax_allsnow	Monthly maximum air temperature when precipitation is assumed to be snow	Climate	˚F	-10 to 40	1, 2
tmax_cbh_adj	Adjustment to maximum air temperature for each HRU, based on slope and aspect	Climate	˚F	-10 to 10	2, 3
tmin_cbh_adj	Adjustment to minimum air temperature for each HRU, based on slope and aspect	Climate	˚F	-10 to 10	2, 3
dday_intcp	Monthly intercept in the degree-day equation	Solar Radiation	dday	-60 to 10	1
dday_slope	Monthly slope in the degree-day equation	Solar Radiation	dday/ ˚F	0.2 to 0.9	1
ppt_rad_adj	Minimum monthly precipitation, if basin precipitation exceeds this value, radiation is multiplied by radj_sppt or radj_wppt	Solar Radiation	inches	0.0 to 0.5	1
radj_sppt	Adjustment factor to computed solar ration for summer days if greater than ppt_rad_adj	Solar Radiation	decimal fraction	0.0 to 1.0	1
radj_wppt	Adjustment factor to computed solar ration for winter days if greater than ppt_rad_adj	Solar Radiation	decimal fraction	0.0 to 1.0	1
radmax	Maximum of the potential solar radiation that may reach the ground	Solar Radiation	decimal fraction	0.1 to 1.0	1, 2
tmax_index	Monthly index temperature used to determine precip. adjustment so solar rad.	Solar Radiation	decimal fraction	-10.0 to 110.0	1
jh_coef	Monthly air temperature coefficient used in the Jensen-Haise potential ET computation	PET	1/ ˚F	0.005 to 0.06	1, 2, 3
jh_coef_hru	Air temperature coefficient used in the Jensen-Haise PET computation by HRU	PET	1/ ˚F	5.0 to 25.0	1, 3
covden_sum	Summer vegetation cover density for the major vegetation type in each HRU	Interception	decimal fraction	0.0 to 1.0	4
covden_win	Summer vegetation cover density for the major vegetation type in each HRU	Interception	decimal fraction	0.0 to 1.0	4
snow_intcp	Snow interception storage capacity for the major vegetation type in each HRU	Interception	inches	0.0 to 1.0	4

srain_intcp	Summer rain interception storage capacity for the major vegetation type in each HRU	Interception	inches	0.0 to 1.0	1, 4
wrain_incp	Winter rain interception storage capacity for the major vegetation type in each HRU	Interception	inches	0.0 to 1.0	1, 4
albset_rna	Fraction of rain in a mixed precipitation event above which the snow albedo is not reset; during snowpack accumulation stage	Snow	decimal fraction	0.4 to 1.0	5
albset_rnm	Fraction of rain in a mixed precipitation event above which the snow albedo is not reset; during snowpack melt stage	Snow	decimal fraction	0.4 to 1.0	5
albset_sna	Minimum snowfall, in water equivalent, needed to reset snow during the snowpack accumulation stage	Snow	inches	0.01 to 1.0	5
albset_snm	Minimum snowfall, in water equivalent, needed to reset snow during the snowpack melt stage	Snow	inches	0.1 to 1.0	5
cecn_coef	Monthly convection condensation energy coefficient	Snow	cal/ ˚C	2.0 to 10.0	1, 2, 3
den_init	Initial density of new-fallen snow	Snow	g/ cm^3	0.01 to 0.5	3
den_max	Average maximum snowpack density	Snow	g/ cm^3	0.1 to 0.8	3
emis_noppt	Average emissivity of air on days without precipitation	Snow	decimal fraction	0.757 to 1.0	1, 2, 3
freeh2o_cap	Free-water holding capacity of snowpack expressed as a decimal fraction of the frozen water content of the snowpack	Snow	decimal fraction	0.01 to 0.2	1, 2
potet_sublim	Fraction of PET that is sublimated from snow in the canopy and snowpack	Snow	decimal fraction	0.1 to 0.75	1, 2, 3
rad_trncf	Transmission coefficient for short-wave radiation through winter vegetation canopy	Snow	decimal fraction	0.0 to 1.0	2, 4
settle_const	Snowpack settlement time constant	Snow	decimal fraction	0.01 to 0.5	3
carea_max	Maximum possible area contributing to surface runoff expressed as a portion of the HRU area	Runoff	decimal fraction	0.0 to 1.0	1, 2, 3
imperv_stor_max	Maximum impervious area retention storage for each HRU	Runoff	inches	0.0 to 0.1	3
smidx_coef	Coefficient in non-linear contributing area algorithm for each HRU	Runoff	decimal fraction	0.001 to 0.06	1, 2, 3
smidx_exp	Exponent in non-linear contributing area algorithm for each HRU	Runoff	1/inch	0.1 to 0.5	1, 3
snowinfil_max	Maximum snow infiltration per day for each HRU	Runoff	inches/ day	0.0 to 20.0	2, 3
fastcoef_lin	Linear coefficient in equation to rout preferential-flow storage down slope for each HRU	Soil zone	frac/day	0.001 to 0.1	1, 2, 3
fastcoef_sq	Non-linear coefficient in equation to rout preferential-flow storage down slope for each HRU	Soil zone	none	0.001 to 1.0	1, 3

pref_flow_den	Fraction of the soil zone in which preferential flow occurs for each HRU: used if control parameter	Soil zone	decimal fraction	0.0 to 1.0	1, 3
sat_threshold	Water holding capacity of the gravity of preferential flow reservoirs; difference between field capacity and total soil saturation for each HRU	Soil zone	inches	1.0 to 999.0	1, 3
slowcoef_lin	Linear coefficient in equation to route gravity reservoir storage down slope by HRU	Soil zone	frac/day	0.001 to 0.5	1, 3
slowcoef_sq	Non-linear coefficient in equation to route gravity reservoir storage down slope by HRU	Soil zone	none	0.001 to 1.0	1, 2, 3
soil2gw_max	Maximum amount of the capillary reservoir excess that is routed directly to the GWR for each HRU	Soil zone	inches	0.0 to 5.0	1, 2
soil_moist_max	Maximum available water holding capacity of capillary reservoir from land surface to rooting depth of the major vegetation type of each HRU	Soil zone	none	0.001 to 10.0	1, 2, 3, 4
soil_rechr_max_frac	Maximum storage for soil recharge zone as fraction of soil_moist_max	Soil zone	decimal fraction	0.1 to 1.0	2
ssr2gw_exp	Non-linear coefficient in equation used to route water from the gravity reservoirs to the GWR for each HRU	Soil zone	none	0.0 to 3.0	1, 2, 3
ssr2gq_rate	Linear coefficient in equation used to route water from the gravity reservoirs to the GWR for each HRU	Soil zone	frac/day	0.05 to 0.8	1, 2, 3
transp_tmax	Temperature index to determine the specific data of the start of transpiration period	Soil zone	˚F	0.0 to 1,000.0	1
gwflow_coef	Linear coefficient in the equation to compute groundwater discharge for each GWR	Groundwater	frac/day	0.001 to 0.5	1, 2, 3

Table S2. General attributes of study basins

Attribute	Blue	Dolores	East	Taylor
Drainage area (km^2)	313.4	1308.0	748.5	331.5
Mean elevation (m)	3355	2956	3131	3328
Outlet elevation (m)	2757	2116	2442	2846
Mean slope (degrees)	16.8	16.4	17.7	14.5
Percent forested (%)	57.1	80.4	48.8	54.3
Mean annual precip. (mm)	700	790	807	676
Mean annual discharge (m^3/s)	2.66	12.1	9.40	3.00
Q/Precip.	0.38	0.37	0.49	0.42
PET/Precip.*	0.46	0.51	0.44	0.48
Latitude at outlet	39.57	37.47	38.66	38.86

*PET calculated using the Thornthwaite method

Table S3. The total number of parameters identified as informative using the Morris method, where the normalized sensitivity measure is above 0.2. The Type I and II sections represent the number of parameters that cross the 0.2 threshold erroneously based on the bootstrap. The letters B, D, E, and T stand for the Blue, Dolores, East, and Taylor catchments.

Variable	Total				Type I				Type II			
	B	D	E	T	B	D	E	T	B	D	E	T
Q	14	12	12	13	4	3	3	1	2	3	2	2
	10	12	12	-	2	2	2	-	3	0	5	-
SWE	9	9	5	9	6	0	5	6	2	1	0	4
	-	9	7	-	-	0	4	-	-	2	0	-
	-	6	-	-	-	1	-	-	-	2	-	-
	-	7	-	-	-	2	-	-	-	1	-	-
	-	7	-	-	-	0	-	-	-	2	-	-
ASO	14	4	11	10	7	2	6	7	2	2	4	2
	14	4	11	10	7	3	6	7	2	2	4	1
	13	4	-	-	6	3	-	-	3	2	-	-
	14	4	-	-	7	3	-	-	2	3	-	-
SCA	9	5	7	9	0	1	0	0	1	1	0	0
SMS2	16	9	11	14	2	1	0	2	4	0	2	0
	-	14	17	-	-	0	3	-	-	1	3	-
SMAP	15	12	16	12	3	0	4	3	1	1	1	3
AET	4	9	10	8	0	0	0	2	3	0	1	1
Unique	22	18	21	19	16	10	13	12	12	11	16	10
All unique	24	22	25	22								

Table S4. Baseline NHM performance in NRMSE, where 0 is best. The lettered subscripts represent individual stations in ascending order based on their numeric site IDs in Figure 2.

Dataset		**Blue**	**Dolores**	**East**	**Taylor**
Q		0.783_{a}	0.514_{a}	0.684_{a}	0.647_{a}
		0.724_{b}	0.462_{b}	0.630_{b}	-
SNOTEL		0.495_{a}	0.357_{a}	0.428_{a}	0.380_{a}
		-	0.404_{b}	0.887_{b}	-
		-	1.21_{c}	-	-
		-	0.625_{d}	-	-
		-	1.05_{e}	-	-
ASO	Apr. 21	3.19	0.587	-	-
	May 21	0.981	0.476	-	-
	Apr. 22	3.13	0.527	0.507	0.652
	May 22	0.958	0.675	1.36	1.04
SCA		2.02	1.81	1.52	1.73
SMS2		1.26_{a}	2.85_{d}	1.15_{a}	1.62_{a}
		-	2.30_{e}	1.31_{b}	-
SMAP		1.72	2.20	2.03	1.85
AET		0.458	0.986	1.21	1.26

References for Supplementary Information

Campolongo, F. and Saltelli, A.: Sensitivity analysis of an environmental model: an application of different analysis methods, Reliability Engineering & System Safety, 57, 49–69, https://doi.org/10.1016/S0951-8320(97)00021-5, 1997.

Campolongo, F., Cariboni, J., and Saltelli, A.: An effective screening design for sensitivity analysis of large models, Environmental Modelling & Software, 22, 1509–1518, https://doi.org/10.1016/j.envsoft.2006.10.004, 2007.

Cuntz, M., Mai, J., Zink, M., Thober, S., Kumar, R., Schäfer, D., Schrön, M., Craven, J., Rakovec, O., Spieler, D., Prykhodko, V., Dalmasso, G., Musuuza, J., Langenberg, B., Attinger, S., and Samaniego, L.: Computationally inexpensive identification of noninformative model parameters by sequential screening, Water Resources Research, 51, 6417–6441, https://doi.org/10.1002/2015WR016907, 2015.

Dingman, S. L.: Physical Hydrology, Waveland Press, Incorporated, 643 pp., 2015.

Gan, Y., Duan, Q., Gong, W., Tong, C., Sun, Y., Chu, W., Ye, A., Miao, C., and Di, Z.: A comprehensive evaluation of various sensitivity analysis methods: A case study with a hydrological model, Environmental Modelling & Software, 51, 269–285, https://doi.org/10.1016/j.envsoft.2013.09.031, 2014.

Hall, D. K., Riggs, G. A., DiGirolamo, N. E., and Román, M. O.: Evaluation of MODIS and VIIRS cloud-gap-filled snow-cover products for production of an Earth science data record, Hydrology and Earth System Sciences, 23, 5227–5241, https://doi.org/10.5194/hess-23-5227-2019, 2019.

Hay, L. E., LaFontaine, J. H., Beusekom, A. E. V., Norton, P. A., Farmer, W. H., Regan, R. S., Markstrom, S. L., and Dickinson, J. E.: Parameter estimation at the conterminous United States scale and streamflow routing enhancements for the National Hydrologic Model infrastructure application of the Precipitation-Runoff Modeling System (NHM-PRMS), Techniques and Methods, U.S. Geological Survey, https://doi.org/10.3133/tm6B10, 2023.

Morris, M. D.: Factorial Sampling Plans for Preliminary Computational Experiments, Technometrics, 33, 161–174, https://doi.org/10.1080/00401706.1991.10484804, 1991.

Salomonson, V. V. and Appel, I.: Estimating fractional snow cover from MODIS using the normalized difference snow index, Remote Sensing of Environment, 89, 351–360, https://doi.org/10.1016/j.rse.2003.10.016, 2004.

Saltelli, A., Ratto, M., Campolongo, F., Cariboni, J., Gatelli, D., Saisana, M., and Tarantola, S.: Elementary Effects Method, in: Global Sensitivity Analysis. The Primer, John Wiley & Sons, Ltd, 109–154, https://doi.org/10.1002/9780470725184.ch3, 2007.

Stillinger, T., Rittger, K., Raleigh, M. S., Michell, A., Davis, R. E., and Bair, E. H.: Landsat, MODIS, and VIIRS snow cover mapping algorithm performance as validated by airborne lidar datasets, The Cryosphere, 17, 567–590, https://doi.org/10.5194/tc-17-567-2023, 2023.